12-26-2019

An Analysis of the Atmospheric Propagation of Underground-Explosion-Generated Infrasonic Waves Based on the Equations of Fluid Dynamics: Ground Recordings

Roberto Sabatini
Embry-Riddle Aeronautical University, SABATINR@erau.edu

Jonathan B. Snively
Embry-Riddle Aeronautical University, snivelyj@erau.edu

Michael P. Hickey
Embry-Riddle Aeronautical University, hicke0b5@erau.edu

J. L. Garrison
Purdue University

Scholarly Commons Citation

Sabatini, R., Snively, J. B., Hickey, M. P., & Garrison, J. L. (2019). An Analysis of the Atmospheric Propagation of Underground-Explosion-Generated Infrasonic Waves Based on the Equations of Fluid Dynamics: Ground Recordings. *The Journal of the Acoustical Society of America, 146*(6). https://doi.org/10.1121/1.5140449

An analysis of the atmospheric propagation of underground-explosion-generated infrasonic waves based on the equations of fluid dynamics: Ground recordings

R. Sabatini, J. B. Snively, M. P. Hickey, and J. L. Garrison

Citation: The Journal of the Acoustical Society of America **146**, 4576 (2019); doi: 10.1121/1.5140449
View online: https://doi.org/10.1121/1.5140449
View Table of Contents: https://asa.scitation.org/toc/jas/146/6
Published by the Acoustical Society of America

An analysis of the atmospheric propagation of underground-explosion-generated infrasonic waves based on the equations of fluid dynamics: Ground recordings

R. Sabatini,[1,a)] J. B. Snively,[1] M. P. Hickey,[1] and J. L. Garrison[2]
[1]*Center for Space and Atmospheric Research and Department of Physical Sciences, Embry-Riddle Aeronautical University, Daytona Beach, Florida 32114, USA*
[2]*School of Aeronautics and Astronautics, Purdue University, West Lafayette 47907, Indiana, USA*

(Received 25 July 2019; revised 22 November 2019; accepted 26 November 2019; published online 26 December 2019)

An investigation on the propagation of underground-explosion-generated infrasonic waves is carried out via numerical simulations of the equations of fluid dynamics. More specifically, the continuity, momentum, and energy conservation equations are solved along with the Herzfeld-Rice equations in order to take into account the effects of vibrational relaxation phenomena. The radiation of acoustic energy by the ground motion caused by underground explosions is initiated by enforcing the equality, at ground level, between the component of the air velocity normal to the Earth's surface and the normal velocity of the ground layer. The velocity of the ground layer is defined semi-empirically as a function of the depth of burial and of the yield. The effects of the depth and of the source energy on the signals recorded in the epicentral zone are first discussed. The tropospheric and stratospheric infrasonic phases traveling at a long-range are then analyzed and explained. Synthesized ground waveforms are finally discussed and compared to those recorded at the I45RU station of the International Monitoring System after the 2013 North-Korean test. Good agreement is found between numerical results and experimental data, which motivates the use of infrasound technologies alongside seismic techniques for the characterization of underground explosions.
 https://doi.org/10.1121/1.5140449

[PBB] Pages: 4576–4591

I. INTRODUCTION

Underground explosions (UEs) generate in the Earth's atmosphere infrasonic waves (Campus and Christie, 2009; Whitaker, 2007, 2008) which can propagate over hundreds or thousands of kilometers (Assink *et al.*, 2016; Campus and Christie, 2009; Che *et al.*, 2014; Koch and Pilger, 2018; Park *et al.*, 2018) and up to the ionosphere (Krasnov and Drobzheva, 2005; Park *et al.*, 2013; Rudenko and Uralov, 1995; Yang *et al.*, 2012). The interest in UE-generated infrasound has received renewed attention in the last decade as a result of the intensification of nuclear activities in the Democratic People's Republic of Korea (DPRK). Between 2006 and 2017, the DPRK has officially conducted six nuclear tests at the Punggye-ri Nuclear Test Site in the northeast of the country (41°16′40″N, 129°05′14″E). These events have all been detected by the international monitoring system (IMS), a network of seismic, radionuclide, hydroacoustic, and infrasonic stations, which has been developed to verify compliance with the Comprehensive Nuclear-Test-Ban Treaty (Koch and Pilger, 2018). Together with seismic data, the infrasonic pressure perturbations recorded by the IMS or other infrasound arrays are believed to provide useful insights for the characterization, in terms of source yield or depth of burial (DOB), of the aforementioned tests. To support this idea, different studies on the North Korean UEs have been recently conducted by using infrasound technologies (Assink *et al.*, 2016; Che *et al.*, 2014; Koch and Pilger, 2018; Park *et al.*, 2018). In particular, Che *et al.* (2014) inferred the acoustic energy released in the epicentral zone of the 2009 UE by analyzing the stratospheric arrivals observed between about a 300 and 500 km distance; Assink *et al.* (2016) investigated the depth of burial (DOB) of the 2013 and the 2016a UEs; Park *et al.* (2018) attempted to estimate the source energy for the test conducted on January 6, 2016. Their analyses were all based on the linear theory of acoustic rays and/or on the parabolic equation method, and most of them implicitly assumed that the acoustic field induced in the atmosphere by a UE can be modeled by an equivalent isotropic point source located on the ground at the epicenter. Characterizing a UE from signals observed at large distances is, however, a complex task, which requires the use of adequate source and propagation models. First of all, while surface and air explosions can be regarded as nearly isotropic emitters of acoustic waves, the energy radiated in the atmosphere by strong UEs is mostly directed upward (Rudenko and Uralov, 1995). This anisotropy in the directivity pattern must be taken into account in quantitative estimations of the source yield from ground recordings. Second, the atmospheric propagation of high-amplitude low-frequency waves is influenced by a large variety of physical phenomena. While it is primarily affected by the refraction induced by temperature and wind vertical gradients (Blom, 2019; Drob *et al.*, 2003; Pierce, 2019; Waxler *et al.*, 2015),

[a)]Current address: Centre for Maritime Research and Experimentation, Science and Technology Organization—NATO, La Spezia, Italy. Electronic mail: roberto87sabatini@gmail.com

the effects of nonlinearity, thermoviscous absorption, diffraction, scattering, and topography play an important role on the signals recorded at long distance from an infrasonic source (de Groot-Hedlin, 2017; Sabatini *et al.*, 2016a; Sabatini *et al.*, 2016b; Sabatini *et al.*, 2019a; Sabatini *et al.*, 2019b). The relaxation of the vibrational degrees of freedom of nitrogen N_2 and oxygen O_2 may also have an impact on the absorption and on the dispersion of acoustic waves of frequency higher than about 1 Hz propagating in stratospheric or tropospheric ducts (Sabatini *et al.*, 2016b).

Over the past decade, significant efforts have been made toward investigations on low-frequency atmospheric waves based on the direct numerical simulation (DNS) of the complete set of the fluid dynamic equations, which are able to capture the aforesaid physical complexity (Bailly and Bogey, 2009; de Groot-Hedlin, 2012, 2016, 2017; Hanique-Cockenpot, 2011; Marsden *et al.*, 2014; Sabatini *et al.*, 2016a; Sabatini *et al.*, 2015, 2019a; Snively, 2013; Zettergren and Snively, 2019). In line with this trend, the objective of the work presently reported is to further develop the DNS approach and to apply it to the study of the infrasonic recordings associated with UEs. To this end, the propagation model discussed in Marsden *et al.* (2014), Sabatini *et al.* (2016a), and Sabatini *et al.* (2019a) is here extended to take into account the effect of the vibrational relaxation of nitrogen N_2 and oxygen O_2. More specifically, the continuity, momentum, and energy conservation equations are integrated along with the Herzfeld-Rice relaxation equations (Pierce, 1978, 2019) as described in Bailly and Bogey (2009) and Hanique-Cockenpot (2011). The infrasonic wave associated with a UE is radiated in the surrounding air by the ground motion induced when the seismic wave generated by the explosive reaches the terrestrial surface. To initiate the infrasonic wave in the atmosphere, the component of the air velocity at a ground level normal to the Earth's surface is therefore set equal to the normal velocity of the ground layer (Rudenko and Uralov, 1995). In keeping with Rudenko and Uralov (1995), this latter velocity is calculated as a function of range and time and depends on the explosion yield, on the DOB as well as on the mechanical properties of the soil (Adushkin and Spivak, 2015; Rudenko and Uralov, 1995). One of the major drawbacks of three-dimensional (3D) DNSs is their computational cost, which dramatically increases as the dominant acoustic wavelength diminishes. In this work, in order to allow for computationally affordable DNSs, the governing equations are rewritten in cylindrical coordinates and axial symmetry is assumed, so that the computations are factually two-dimensional, while the acoustic field remains 3D.

In the present paper, four important questions are addressed: (1) the effects of the explosion yield and of the DOB on the acoustic wavefront radiated in the atmosphere is first analyzed; (2) the influence of the anisotropy in the directivity of the radiated wave on the signals traveling in the different atmospheric ducts is then highlighted; (3) an investigation of the tropospheric and stratospheric infrasonic signals recorded after the 2013 North Korean test at the I45RU station of the IMS is also realized, and a qualitative comparison with the data described in Assink *et al.* (2016) is performed; and (4) the impact of the vibrational relaxation of nitrogen N_2 and oxygen O_2 on the acoustic field generated by this event is finally examined. In order to investigate these points, different direct numerical simulations are carried out.

The paper is organized as follows. The set of equations and the source implementation are presented in Sec. II, along with a discussion on the main assumptions of the present propagation model. The parameters of the computations and the numerical method are then described in Sec. III. Section IV is devoted to the analysis of the results. Concluding remarks are finally drawn in Sec. V.

II. MODELING OF THE PROPAGATION OF INFRASONIC WAVES GENERATED BY UNDERGROUND EXPLOSIONS

The present investigation involves computing the 3D axisymmetric acoustic field generated by a UE in the Earth's atmosphere. A cylindrical coordinate system $Or\vartheta z$ with its origin at the epicenter of the UE is employed [cf. Fig. 1(a)] and, for the purpose of the present investigation, the Earth's surface is considered flat.

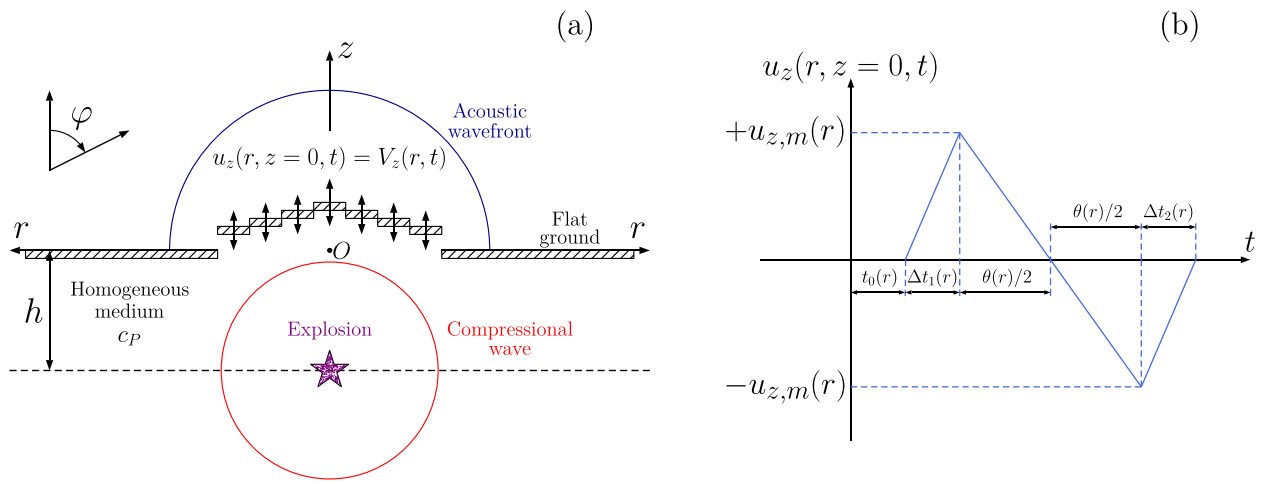

FIG. 1. (Color online) (a) Sketch of the problem. (b) Ground vertical velocity profile at a given instant of time.

A. Propagation model

Air is assumed to behave as an ideal gas mixture satisfying the equation of state $p = \rho \mathcal{R} T$, where p is the pressure, ρ is the density, T is the temperature, and $\mathcal{R} = 287.06\ \mathrm{J\,kg^{-1}\,k^{-1}}$ is the specific gas constant.

1. Initial unperturbed atmosphere

The initial unperturbed atmosphere is defined as a stratified medium at rest and it is constructed by specifying the speed-of-sound vertical profile $\bar{c}(z)$. The effect of horizontal winds is included in the function $\bar{c}(z)$ by using the effective-celerity approximation, which is generally accurate if the angle between the propagation wavenumber vector and the flow direction is small (Godin, 2002). As described in Sec. IV, this condition is verified for the tropospheric and stratospheric arrivals under investigation. The mean temperature $\bar{T}(z)$ is computed as $\bar{T}(z) = \bar{c}^2(z)/(\gamma \mathcal{R})$, where $\gamma = 1.4$ represents the ratio of specific heats calculated as if all the vibrational degrees of freedom of the gas molecules were frozen (Pierce, 1978). The atmospheric pressure $\bar{p}(z)$ is obtained from the hydrostatic equilibrium equation

$$\frac{d\bar{p}}{dz} = -\bar{\rho} g = -\frac{g}{\mathcal{R}\bar{T}}\bar{p}, \tag{1}$$

where $g = 9.81\ \mathrm{m\,s^{-2}}$ is the gravitational acceleration, which is integrated numerically from $z = 0$ km with $\bar{p}(0) = p_{\mathrm{ref}} = 101\,325$ Pa. The density profile $\bar{\rho}(z)$ is finally determined from the equation of state, $\bar{\rho} = \bar{p}/(\mathcal{R}\bar{T})$.

2. Governing equations

Wave propagation is governed by the continuity, momentum, and energy conservation equations, along with the Herzfeld-Rice equations (Bailly and Bogey, 2009; Hanique-Cockenpot, 2011; Pierce, 1978), which take into account the effect of the vibrational relaxation of nitrogen N_2 and oxygen O_2. Assuming axial symmetry, they can be recast as

$$\begin{aligned}
\frac{\partial \rho}{\partial t} &= -\frac{1}{r}\frac{\partial (r\rho u_r)}{\partial r} - \frac{\partial(\rho u_z)}{\partial z},\\
\frac{\partial(\rho u_r)}{\partial t} &= -\frac{1}{r}\frac{\partial (r(\rho u_r u_r + p))}{\partial r} - \frac{\partial(\rho u_r u_z)}{\partial z} + \frac{p}{r} + \frac{1}{r}\frac{\partial(r\tau_{rr})}{\partial r} + \frac{\partial \tau_{rz}}{\partial z} - \frac{\tau_{\vartheta\vartheta}}{r},\\
\frac{\partial(\rho u_z)}{\partial t} &= -\frac{1}{r}\frac{\partial (r\rho u_r u_z)}{\partial r} - \frac{\partial(\rho u_z u_z + p)}{\partial z} - \rho' g + \frac{1}{r}\frac{\partial(r\tau_{rz})}{\partial r} + \frac{\partial \tau_{zz}}{\partial z},\\
\frac{\partial(\rho e_{t,\mathrm{tr-rot}})}{\partial t} &= -\frac{1}{r}\frac{\partial \big(r(\rho e_{t,\mathrm{tr-rot}} + p)u_r\big)}{\partial r} - \frac{\partial\big((\rho e_{t,\mathrm{tr-rot}} + p')u_z\big)}{\partial z} - \bar{p}\frac{\partial u_z}{\partial z} - \rho' g u_z\\
&\quad + \frac{1}{r}\frac{\partial(r(u_r\tau_{rr} + u_z\tau_{rz} - q_r^\star))}{\partial r} + \frac{\partial(u_r\tau_{rz} + u_z\tau_{zz} - q_z^\star)}{\partial z} - \sum_\beta c_{v\beta}\frac{\rho T - \rho T_\beta}{\Theta_\beta},\\
\frac{\partial(\rho T_\beta)}{\partial t} &= -\frac{1}{r}\frac{\partial\big(r\rho T_\beta u_r\big)}{\partial r} - \frac{\partial(\rho T u_z)}{\partial z} + \frac{\rho T - \rho T_\beta}{\Theta_\beta}.
\end{aligned} \tag{2}$$

The variable u_r and u_z represent the radial and vertical components of the velocity vector, $p' = p - \bar{p}$ is the pressure perturbation, $\rho' = \rho - \bar{\rho}$ is the density perturbation, τ_{rr}, τ_{rz}, τ_{zz}, and $\tau_{\vartheta\vartheta}$ are the viscous stresses, and $q_r^\star$ and $q_z^\star$ are the heat fluxes. The term $e_{t,\mathrm{tr-rot}}$ indicates the total energy per unit mass computed by including only the internal energies associated with the translational and rotational degrees of freedom of the gas molecules (Pierce, 1978). It is related to the other flow variables by the following formula:

$$e_{t,\mathrm{tr-rot}} = \frac{p}{\rho(\gamma - 1)} + \frac{1}{2}(u_r^2 + u_z^2). \tag{3}$$

Finally, T_β, Θ_β, and $c_{v\beta}$ are the vibrational temperature, the relaxation time and the relaxation specific heat at constant volume of the species β, respectively.

Note that, in keeping with Marsden *et al.* (2014), the hydrostatic equilibrium condition for the initial unperturbed atmosphere, $d\bar{p}/dz = -\bar{\rho} g$, is here subtracted from the equations in order to bypass its high-precision computation at each time step.

The viscous stresses are calculated as

$$\begin{aligned}
\tau_{rr} &= 2\mu\frac{\partial u_r}{\partial r} + \left[\mu_v - \frac{2}{3}\mu\right]\left[\frac{1}{r}\frac{\partial(ru_r)}{\partial r} + \frac{\partial u_z}{\partial z}\right],\\
\tau_{zz} &= 2\mu\frac{\partial u_z}{\partial z} + \left[\mu_v - \frac{2}{3}\mu\right]\left[\frac{1}{r}\frac{\partial(ru_r)}{\partial r} + \frac{\partial u_z}{\partial z}\right],\\
\tau_{\vartheta\vartheta} &= 2\mu\frac{u_r}{r} + \left[\mu_v - \frac{2}{3}\mu\right]\left[\frac{1}{r}\frac{\partial(ru_r)}{\partial r} + \frac{\partial u_z}{\partial z}\right],\\
\tau_{rz} &= \mu\left[\frac{\partial u_r}{\partial z} + \frac{\partial u_z}{\partial r}\right].
\end{aligned} \tag{4}$$

The dynamic viscosity μ depends on the temperature T and is given by the expression

$$\mu(T) = \mu_{\mathrm{ref}}\left(\frac{T}{T_{\mathrm{ref}}}\right)^{3/2}\frac{T_{\mathrm{ref}} + T_S}{T + T_S}, \tag{5}$$

where $\mu_{\text{ref}} = 1.8192 \times 10^{-5}$ Pa s, $T_{\text{ref}} = 293.15$ K, and $T_S = 117$ K (Sutherland and Bass, 2004, 2006). The bulk viscosity μ_v is generally expressed as a function of μ. For the range of temperatures of interest in this paper, the ratio μ_v/μ varies slowly and, in keeping with Pierce (1978), it is assumed constant and equal to $\mu_v/\mu = 0.6$. This value is confirmed by the recent studies by Cramer (2012) and Li *et al.* (2017).

In order to avoid the diffusion of the initial atmospheric state during the acoustic propagation, the heat fluxes are computed from the perturbation of temperature $T' = T - \bar{T}$

$$q_r^\star = -\lambda \frac{\partial T'}{\partial r}; \quad q_z^\star = -\lambda \frac{\partial T'}{\partial z}. \tag{6}$$

In these formulas, the thermal conductivity λ is given by

$$\lambda = \frac{\mu c_p}{\text{Pr}}, \tag{7}$$

where $c_p = \gamma \mathcal{R}/(\gamma - 1)$ is the specific heat at constant pressure and $\text{Pr} = 0.72$ is the fluid's Prandtl number.

The relaxation specific heat at constant volume $c_{v\beta}(T_\beta)$ is expressed by the relation

$$c_{v\beta}(T_\beta) = X_\beta \mathcal{R} \left(\frac{T_\beta^{\text{ref}}}{T_\beta}\right)^2 e^{-T_\beta^{\text{ref}}/T_\beta}, \tag{8}$$

where X_β is the mole fraction of the species β (assumed constant here) and T_β^{ref} is a characteristic temperature associated with molecular vibrations. In the present investigation, the relaxation processes of nitrogen N_2 and oxygen O_2 are considered. Their mole fractions and characteristic temperatures are: $X_{N_2} = 0.78$, $X_{O_2} = 0.21$, $T_{N_2}^{\text{ref}} = 3352$ K, and $T_{O_2}^{\text{ref}} = 2239.1$ K. The relaxation times Θ_{N_2} and Θ_{O_2} depend on the pressure, on the temperature and on the humidity, among other factors (Pierce, 1978). For the purpose of the present investigation, they are calculated through the following simplified expressions:

$$\begin{aligned} \Theta_{N_2} &= \frac{1}{2\pi\alpha_{N_2}} \frac{p_{\text{ref}}}{p} \left(\frac{T}{T_{\text{ref}}}\right)^{1/2}, \\ \Theta_{O_2} &= \frac{1}{2\pi\alpha_{O_2}} \frac{p_{\text{ref}}}{p}, \end{aligned} \tag{9}$$

with $\alpha_{N_2} = 9$ s and $\alpha_{O_2} = 24$ s, where the effect of tropospheric humidity is neglected (Pierce, 1978).

Finally, the radiation of energy from a UE is modeled by enforcing, for $z = 0$, the equality between the fluid's velocity u_z and the ground vertical velocity V_z induced by the UE

$$u_z(r, z = 0, t) = V_z(r, t). \tag{10}$$

An expression for the function $V_z(r,t)$ is described in the following paragraph.

B. Ground motion induced by an underground explosion

An explosion is considered underground when the ratio $h/Q^{1/3}$ between the DOB h and the explosive yield Q exceeds the value of 5 m kt$^{-1/3}$ (Adushkin and Spivak, 2015). When a nuclear weapon is exploded under the ground, a sphere of hot and high-pressure gases is formed. The expansion of the gas bubble induces an intense compressional wave which propagates in the surrounding rock. When the upwardly directed shock (compression) reaches the Earth's surface, it is reflected back as a rarefaction or tension wave. If its amplitude exceeds the rupture strength of the rock, the surface will spall (Glasstone and Dolan, 1977). As a result of the momentum imparted by the incident wave, the spalled layers move upward and then fall back under the effect of gravity. The ground motion of the spalled surface radiates acoustic energy in the atmosphere. Shear, Rayleigh, Love, and successive compressional waves can be observed as well (Rodean, 1970), however, the initial shock is assumed to constitute the principal contribution to the atmospheric acoustic field in the epicentral zone of the UE.

The ground vertical velocity $V_z(r,t)$ induced by a UE depends on the yield Q, on the DOB h, on the distance from the epicenter r, and, finally, on the properties of the rock. Various models exist for the estimation of the function $V_z(r,t)$ (Jones *et al.*, 2015; Lee and Walker, 1980; Rudenko and Uralov, 1995). Loosely speaking, they implicitly suppose that the velocity $V_z(r,t)$ can be expressed as the sum of a dominant term and an irregular component associated with the local inhomogeneities of the ground medium. The first one can be presumably deduced by assuming that the Earth's surface is flat and that the aforesaid initial compressional wave is spherical and propagates in a homogeneous medium [cf. Fig. 1(a)]. The second one causes the apparent complexity exhibited in measured signals $V_z(r,t)$, but plays a minor role on the evolution of the acoustic wave emitted in the atmosphere (Lee and Walker, 1980).

In this work, the model proposed by Rudenko and Uralov (1995) is employed. The spherical shock originated from the explosion center arrives, at a given distance r on the ground, at the instant $t_0(r)$

$$t_0(r) = \frac{\sqrt{r^2 + h^2}}{\bar{c}_P}, \tag{11}$$

where the variable $\bar{c}_P$ represents the speed of the P waves in the rock. For granite, which is the main constituent of the North Korean soil, the celerity $\bar{c}_P$ is equal to $\bar{c}_P = 5870$ m s^{-1}. The terrestrial surface is detached and lifted up, and reaches its maximum velocity $V_{z,m}(r) \equiv \max_t(V_z(r,t))$ in a very short time $\delta t_1(r)$, also called rise time. This latter is comparable to the duration θ^+ of the compressive phase of the P wave. Here, it is assumed to be independent of the distance r and is taken equal to $\delta t_1 = \theta^+/2$, where the value of θ^+ for granite is computed as

$$\theta^+ = 4.7 \times 10^{-5} \text{ s kg}^{-1/3} \times Q^{1/3}. \tag{12}$$

The maximum velocity $V_{z,m}(r)$ is given by the empirical formula

$$V_{z,m}(r) = \beta \left(\frac{Q^{1/3}}{\sqrt{r^2 + h^2}}\right)^\chi, \tag{13}$$

where the exponent χ is determined experimentally and it is usually assumed to be equal to $\chi = 1.6$, whereas the coefficient β depends on the type of rock and has a value of $\beta = 10$ for hard granite and basalt. The initial sharp acceleration is followed by a period of free fall: the detached soil layer falls under the effect of the gravitational force and the ground velocity evolves according to the equation

$$\frac{\partial V_z(r,t)}{\partial t} = -g. \tag{14}$$

The free-flight duration $\theta(r)$ is a function of the distance r and is computed as

$$\theta(r) = 2\frac{V_{z,m}(r)}{g}. \tag{15}$$

The free fall ends when the spalled layer returns to its original position. During the impact with the ground, the vertical velocity of the lifted soil varies from $-V_{z,m}(r)$ to 0 in a very short time $\delta t_2(r)$. The duration $\delta t_2(r)$ is approximately equal to $\Delta h/\bar{c}_P$, where Δh is the thickness of the detached layer. However, according to Rudenko and Uralov (1995), accurate values of δt_2 are unnecessary to determine the atmospheric pressure signal, especially in the zone of main acoustic radiation, where $\delta t_2 \ll \theta(r)$. As a consequence, in keeping with Rudenko and Uralov (1995), the parameter δt_2 is taken equal to $\delta t_2 = \delta t_1/2 = \theta^+/4$.

In summary, the ground vertical velocity is expressed as

$$V_z(r,t) = \begin{cases} V_{z,m}(r)\dfrac{t_r(r)}{\delta t_1}, & 0 \le t_r(r) \le \delta t_1, \\ V_{z,m}(r) - g[t_r(r) - \delta t_1], & \delta t_1 \le t_r(r) \le [\delta t_1 + \theta(r)], \\ V_{z,m}(r)\dfrac{t_r(r) - \delta t_1 - \theta(r) - \delta t_2}{\delta t_2}, & [\delta t_1 + \theta(r)] \le t_r(r) \le [\delta t_1 + \theta(r) + \delta t_2], \\ 0, & \text{otherwise}, \end{cases} \tag{16}$$

where $t_r(r) = t - t_0(r)$ is the retarded time. For the given soil parameters, the velocity $V_z(r,t)$ is completely defined by specifying the source yield Q and the DOB h. Rudenko and Uralov (1995) further define an optimal DOB as a function of Q: $h = h_{\text{opt}} = 1.43\,\text{m}\,\text{kg}^{-1/3}\,Q^{1/3}$; as an illustration, $h = h_{\text{opt}} \simeq 308\,\text{m}$ for $Q = 10\,\text{kt}$.

C. About the main assumptions of the present propagation model

The present propagation model relies upon three main hypotheses, namely the flatness of the ground, the rotational symmetry of the acoustic field and the laminarity of the atmospheric flow.

The topography could introduce variations in the normal velocity to the Earths's surface and could eventually affect the wavefront emitted in the atmosphere. Mountains and hills could influence the tropospheric waveguide as well, as also discussed by de Groot-Hedlin (2017). On the contrary, they should have a negligible effect on the stratospheric arrivals, which travel at altitudes much higher than the characteristic height of terrestrial mounts.

Since the atmospheric acoustic field is considered axisymmetric, the effect of horizontal winds along the propagation axis is included in the function $\bar{c}(z)$ by using the effective-speed-of-sound approximation. Such an approximation is generally accurate if the angle between the wavenumber vector and the flow direction is small (Godin, 2002). As described in Sec. IV, this condition is verified for the tropospheric and stratospheric arrivals under investigation. The assumption of rotational symmetry of the pressure field implies, however, the neglect of crosswinds, which could have an impact on the amplitudes of the infrasonic phases and be responsible for additional arrivals.

Finally, the atmospheric flow is here assumed laminar. As demonstrated by a recent study conducted by the authors (cf. Sabatini *et al.*, 2019b), among others, turbulent fluctuations scatter the traveling infrasonic waves and potentially modify the ground recordings.

Despite the present simplifications, the main conclusions drawn in Sec. IV are expected to hold true in reality. Nevertheless, the aforementioned assumptions have to be relaxed in the future to improve the description of the acoustic field generated by underground explosions.

III. PARAMETERS OF THE SIMULATIONS AND NUMERICAL METHOD

In this study, eleven simulations are carried out. They are labeled as NF1kt, NF10kt, NF100kt, NF10ktS, NF10ktD, NF2013A, FF2013A, NF2013B, FF2013B, FF2013AWR, and NF2013A4m, where the acronyms NF and FF stand for *near field* and *far field*, respectively. The first five computations are performed in order to study the effect of the source yield and of the DOB on the acoustic field observed near the epicenter of a UE. More specifically, simulations NF1kt, NF10kt, and NF100kt are realized with a constant DOB, $h = h_{\text{opt}}$, and with $Q = 1\,\text{kt}, Q = 10\,\text{kt}$, and $Q = 100\,\text{kt}$, respectively, whereas cases NF10ktS and NF10ktD are investigated with a fixed source yield, $Q = 10\,\text{kt}$, and with $h = 0.5h_{\text{opt}}$ and $h = 2.0h_{\text{opt}}$.

For these five computations, the initial unperturbed atmosphere is an isothermal medium, where the effective speed of sound is taken equal to $\bar{c} = 340\ \mathrm{m\,s^{-1}}$. Simulations NF2013A, FF2013A, NF2013B, and FF2013B are performed in order to examine the acoustic near and far fields induced by the underground test conducted in North Korea on 12 February 2013 and to analyze the subsequent ground infrasonic signal recorded at the I45RU station of the IMS [cf. Fig. 2(a)]. The source yield has been estimated between about 8.4 and 16 kt and the DOB has been evaluated between around 420 and 480 m (Assink *et al.*, 2016; Voytan *et al.*, 2019; Zhang and Wen, 2013). Therefore, the parameter Q is chosen to be equal to $Q = 8$ kt for the cases NF2013A and FF2013A, and to $Q = 16$ kt for the configurations NF2013B and FF2013B. In these four computations, the DOB is set equal to $h = 450$ m. Simulation FF2013AWR (WR stands for *without relaxation*) aims at investigating the effect of the vibrational relaxation of nitrogen N_2 and oxygen O_2. In this case, $Q = 8$ kt and $h = 450$ m. Finally, computation NF2013A4m is carried out for a convergence analysis, as explained in Appendix B. For the last six simulations, the effective speed-of-sound profile is constructed from ECMWF data and is illustrated in Fig. 2(b). The parameters of the computations are summarized in Table I.

The near-field simulations are performed on a square of sizes $L_r^{\mathrm{phys}} = L_z^{\mathrm{phys}} = 8$ km, with $r, z \in [0, 8]$ km. In the far-field computations, the physical domain of interest has sizes $L_r^{\mathrm{phys}} = 450$ km, $L_z^{\mathrm{phys}} = 60$ km, for $r \in [0, 450]$ km, and $z \in [0, 60]$ km. Due to limitations in computational resources, a moving frame is employed, as also done in previous studies (de Groot-Hedlin, 2016; Sabatini *et al.*, 2015, 2019a; Salomons *et al.*, 2002). The fluid dynamic Eq. (2) are solved only in a narrow region, covering a horizontal distance of 106.488 km, which moves along the r-axis and follows the acoustic wavefront. Its displacement is activated as soon as the upward propagating portion of the acoustic wavefront exits the computational domain through the top boundary (for instance, see Fig. 9).

The numerical computations are carried out on a structured grid, consisting of $N_r \times N_z$ mesh nodes on the r- and z-axes, by using a low-dispersive and low-dissipative explicit high-order finite-difference time-domain method (Berland *et al.*, 2007; Bogey and Bailly, 2004; Bogey *et al.*, 2009). Fourth-order 11-point stencil schemes with a resolution of five points-per-wavelength are used for the computation of the spatial derivatives (Berland *et al.*, 2007; Bogey and Bailly, 2004). A second-order, six-stage Runge-Kutta algorithm with low levels of dissipation and dispersion up to four points-per-period is implemented for the integration in time (Bogey and Bailly, 2004). At the end of each time step, spatial low pass filtering is performed in order to damp out the non-resolved wavenumbers. For this purpose, an explicit sixth-order 11-point stencil filter, designed to remove fluctuations discretized by less than four grid points per wavelength, while leaving larger wavelengths unaffected, is used (Bogey *et al.*, 2009). Additionally, a shock-capturing procedure is employed to handle the acoustic shocks generated during the propagation (Bogey *et al.*, 2009). The terms that are proportional to $1/r$ in Eqs. (2) are singular on the axis z and a specific numerical treatment is required to avoid divergent results. In this work, the strategy proposed by Mohseni and Colonius (2000) is adopted: the radial coordinate r is extended toward negative radius; the computational grid is then defined on a set of nodes which exclude the origin $r = 0$, i.e.,

$$r_i = \frac{(2i+1)\Delta r}{2}, \quad i = -5, \ldots, (N_r - 6); \tag{17}$$

only five points with negative range are needed since the stencil of the finite-difference schemes here employed is of 11 nodes; symmetry conditions are finally applied for the nodes with negative range

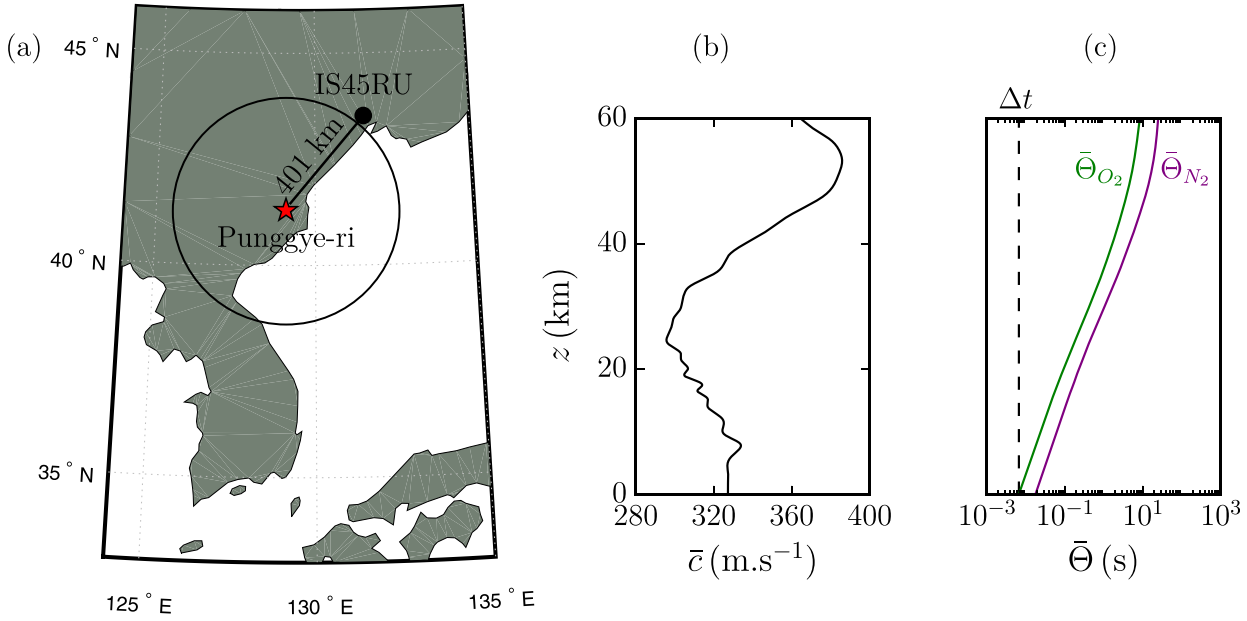

FIG. 2. (Color online) (a) Map of the North-Korean region, which illustrates the locations of the Punggye-ri Nuclear Test Site and of the I45RU infrasound station of the IMS, located in Russia at 401 km from UE position. (b) Effective speed-of-sound profile employed for simulations NF2013A, FF2013A, NF2013B, FF2013B, FF2013AWR, and NF2013A4m. (c) Relaxation times of nitrogen N_2 (purple line) and oxygen O_2 (green line); the dashed line indicates the value of the temporal step Δt.

TABLE I. Parameters of the eleven simulations performed in the present work.

Simulation	Q	h	$\bar{c}$	$\Delta r = \Delta z$	Δt	Relaxation effects
NF1kt	1 kt	$h_{\text{opt}} = 143$ m	340 m.s^{-1}	2 m	0.00167 s	Included
NF10kt	10 kt	$h_{\text{opt}} \simeq 308$ m	340 m.s^{-1}	2 m	0.00167 s	Included
NF100kt	100 kt	$h_{\text{opt}} \simeq 664$ m	340 m.s^{-1}	2 m	0.00167 s	Included
NF10ktD	10 kt	$2.0h_{\text{opt}} \simeq 616$ m	340 m.s^{-1}	2 m	0.00167 s	Included
NF10ktS	10 kt	$0.5h_{\text{opt}} \simeq 154$ m	340 m.s^{-1}	2 m	0.00167 s	Included
NF2013A	8 kt	450 m	Figure 2(b)	2 m	0.00167 s	Included
FF2013A	8 kt	450 m	Figure 2(b)	8 m	0.00670 s	Included
8NF2013B	16 kt	450 m	Figure 2(b)	2 m	0.00167 s	Included
FF2013B	16 kt	450 m	Figure 2(b)	8 m	0.00670 s	Included
FF2013AWR	8 kt	450 m	Figure 2(b)	8 m	0.00670 s	Not included
NF2013A4m	8 kt	450 m	Figure 2(b)	4 m	0.00334 s	Included

$$
\begin{aligned}
&\rho(r_i,z,t) = +\rho(r_{-i-1},z,t),\\
&\rho(r_i,z,t)u_r(r_i,z,t) = -\rho(r_{-i-1},z,t)u_r(r_{1-i},z,t),\\
&\rho(r_i,z,t)u_z(r_i,z,t) = +\rho(r_{-i-1},z,t)u_z(r_{1-i},z,t),\\
&\rho(r_i,z,t)e_{t,\text{tr}-\text{rot}}(r_i,z,t) = +\rho(r_{-i-1},z,t)e_{t,\text{tr}-\text{rot}}(r_{1-i},z,t),\\
&\rho(r_i,z,t)T_{N_2}(r_i,z,t) = +\rho(r_{-i-1},z,t)T_{N_2}(r_{1-i},z,t),\\
&\rho(r_i,z,t)T_{O_2}(r_i,z,t) = +\rho(r_{-i-1},z,t)T_{O_2}(r_{1-i},z,t),
\end{aligned}
\qquad i = -5,\ldots,-1\,. \tag{18}
$$

At grid points near the top and the right boundaries of the computational domain, radiation conditions, as formulated by Bogey and Bailly (2002), are implemented. In the far-field simulations, once the horizontal displacement of the moving frame is activated, these radiation conditions are applied as well at nodes near the left boundary. Finally, to diminish the amplitude of the outgoing waves reaching the top edge and to prevent significant spurious reflections, the physical domain of interest ($z \leq 60$ km) is extended (for $z > 60$ km) through a top sponge layer, where a highly-dissipative Laplacian filter is employed.

The near-field simulations are performed with grid spacings equal to $\Delta r = \Delta z = 2$ m and with a time step of $\Delta t = 0.0017$ s, whereas $\Delta r = \Delta z = 8$ m and $\Delta t = 0.0067$ s for the far-field computations. A discussion about the accuracy allowed by this choice of the spatial step for the cases under study is provided in Appendix B. The temporal step is constrained not only by stability requirements but also by the need for correctly taking into account the relaxation terms in System 2. Indeed, as shown by Hanique-Cockenpot (2011) and as reported in Appendix A, the parameter Δt should be everywhere lower than about $1.55\bar{\Theta}$, where $\bar{\Theta}$ is the minimum value of the different relaxation times. The variables $\bar{\Theta}_{N_2}(z)$ and $\bar{\Theta}_{O_2}(z)$, computed from formulas [Eq. (9)] by using the atmospheric pressure $\bar{p}$ and the atmospheric temperature $\bar{T}$, are plotted in Fig. 2 as functions of altitude. The choice $\Delta t = 0.0067$ s for the far-field simulations allows for verifying the aforementioned accuracy condition for all altitudes z.

To conclude, the numerical algorithm is implemented in the OpenCL language and runs on a NVIDIA Tesla P100 GPU with a memory allocation limit of 16 GB. The computational cost for the most demanding simulations, i.e., the far-field cases, which require around 210 000 time-steps, is of about five days.

IV. RESULTS

A. Analysis of the acoustic field observed near the epicenter of an underground explosion for different yields and DOBs

The scaled pressure perturbations $\Phi = p'/\sqrt{\bar{\rho}}$ obtained in the case NF10kt at three different times, $t = 1.67$ s, $t = 8.3$

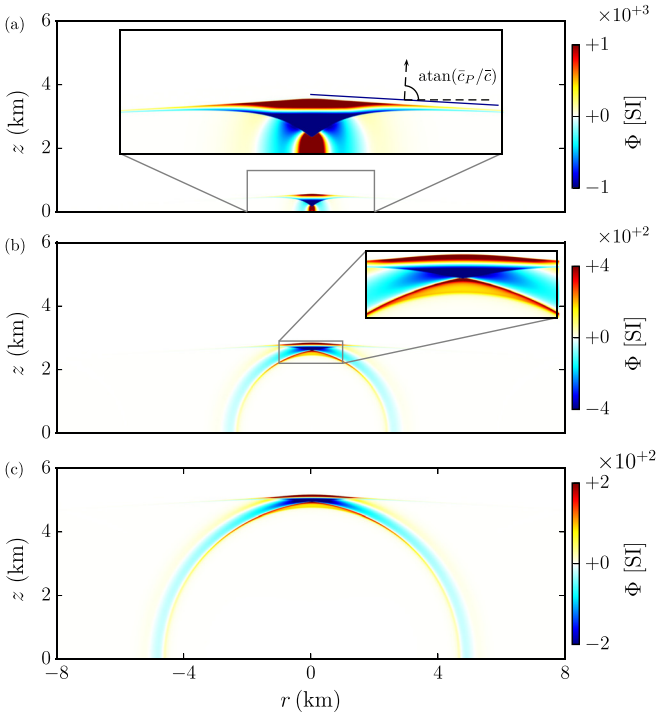

FIG. 3. (Color online) Scaled pressure field Φ obtained for case NF10 kt at three different times: (a) $t = 1.67$ s, (b) $t = 8.3$ s, (c) $t = 15$ s.

s, and $t = 15$ s, are reported in Figs. 3(a)–3(c). The pressure field appears as a superposition of two distinct fronts: a planar front, corresponding to the refracted P wave and traveling with an angle of $\mathrm{atan}(\bar{c}_P/\bar{c}) \simeq 86.685°$ with respect to the horizontal axis, and a spherical front emanating from the epicentral point. The amplitude of the planar front rapidly decays far from the vertical axis. As a result of the high source yield, the propagation is nonlinear and shocks rapidly form. Moreover, the wave is clearly nonisotropic, as most of the acoustic energy is directed upward [cf. Fig. 3(c)].

The scaled pressure signals Φ obtained in the near-field cases at a distance $R_{\mathrm{NF}} = \sqrt{r_{\mathrm{NF}}^2 + z_{\mathrm{NF}}^2}$ of 5 km from the epicenter and for zenith angles $\varphi_{\mathrm{NF}} = \mathrm{atan}(r_{\mathrm{NF}}/z_{\mathrm{NF}})$ equal to $\varphi_{\mathrm{NF}} = 0°, 30°, 60°, 90°$, are reported on the left sides of Figs. 4 and 5. The corresponding one-sided energy spectral densities $\mathrm{ESD}(\Phi)$, defined by the formula

$$\mathrm{ESD}(\Phi) = 2\int_{-\infty}^{+\infty} \Phi(r,z,t)e^{-i2\pi ft}dt \quad f \in \mathbb{R}^+ \tag{19}$$

are illustrated on the right. Both the yield and the DOB have a marked effect on the shape and on the amplitude of these signals. Nevertheless, some general conclusions can be drawn. An N-like waveform is observed for $\varphi_{\mathrm{NF}} = 0°$, on the vertical axis [cf. Fig. 4(a)]. Both its duration and its amplitude increase as the explosion yield augments and as the DOB diminishes. More specifically, the time intervals

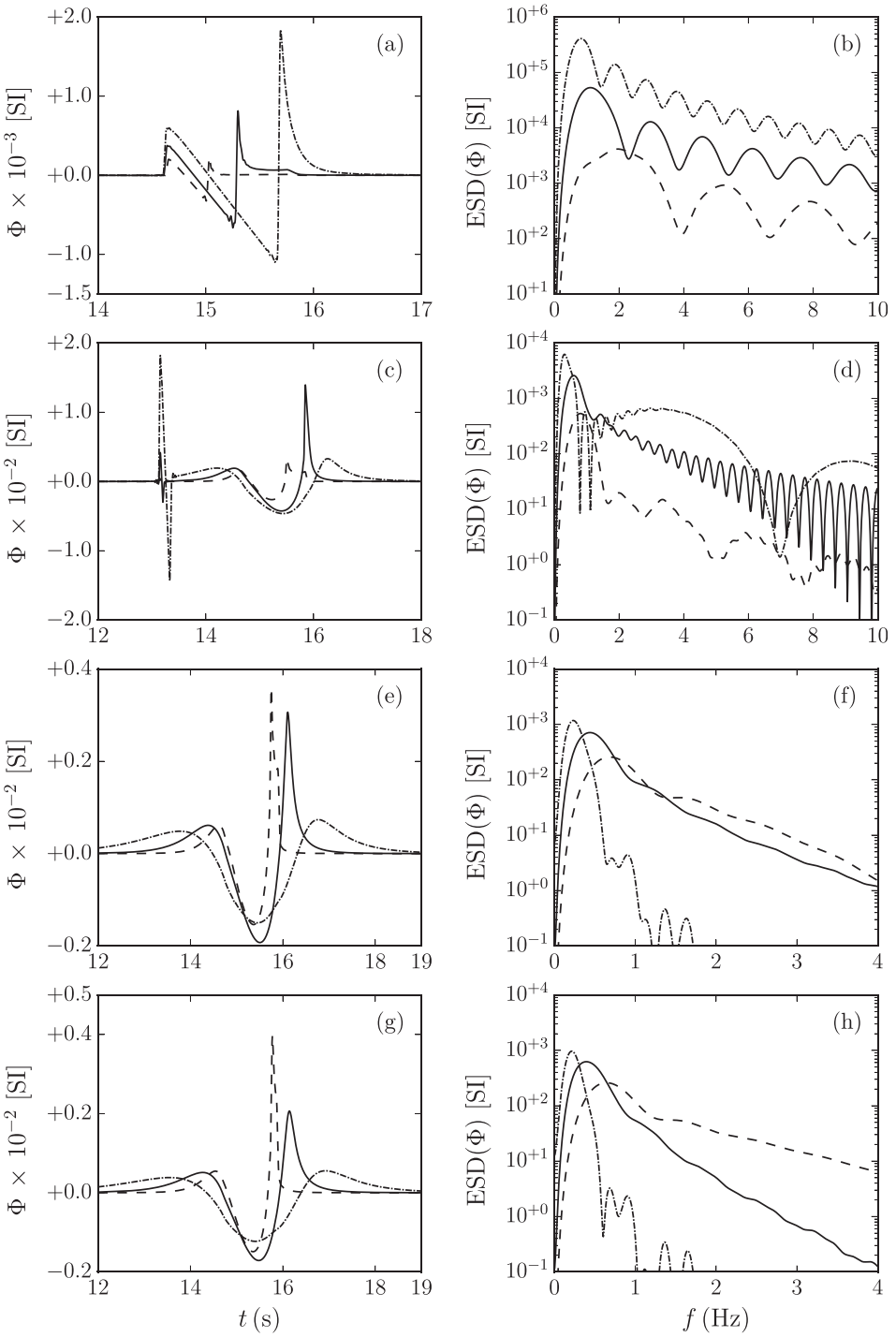

FIG. 4. Signals Φ synthesized at 5 km distance from the epicenter and corresponding one-sided energy spectral densities $\mathrm{ESD}(\Phi)$ for (a) and (b) $\varphi_{\mathrm{NF}} = 0°$, (c) and (d) $\varphi_{\mathrm{NF}} = 30°$, (e) and (f) $\varphi_{\mathrm{NF}} = 60°$, and (g) and (h) $\varphi_{\mathrm{NF}} = 90°$: (dashed line) case NF1kt, (solid line) case NF10kt, (dashed-dotted line) case NF100kt.

TABLE II. Characteristics of the signals obtained in cases NF1kt, NF10kt, NF100kt, NF10ktS and NF10ktD, for $R_{NF} = 5$ km and $\varphi_{NF} = 0^\circ$.

Simulation	N-wave duration (s)	Dominant frequency (Hz)	Maximum of ESD(Φ) (SI)
NF1kt	0.39	1.960	4.15×10^3
NF10kt	0.67	1.110	5.32×10^4
NF100kt	1.05	0.824	4.08×10^5
NF10ktD	0.44	1.920	7.36×10^3
NF10ktS	0.75	0.944	7.41×10^4

between the front and rear shocks are equal to about 0.39, 0.67, 1.05, 0.44, and 0.75 s for cases NF1kt, NF10kt, NF100kt, NF10ktD, and NF10ktS, respectively. The corresponding dominant frequencies are around 1.96, 1.11, 0.824, 1.92, and 0.944 Hz, respectively. These results are summarized in Table II.

In all cases, the amplitude of the scaled pressure signals Φ associated with the spherical front rapidly decreases as φ_{NF} varies from 0° to 90°. As an example, the maximum value of the function ESD(Φ) at $\varphi_{NF} = 30^\circ$ can be more than ten times smaller than the corresponding value obtained

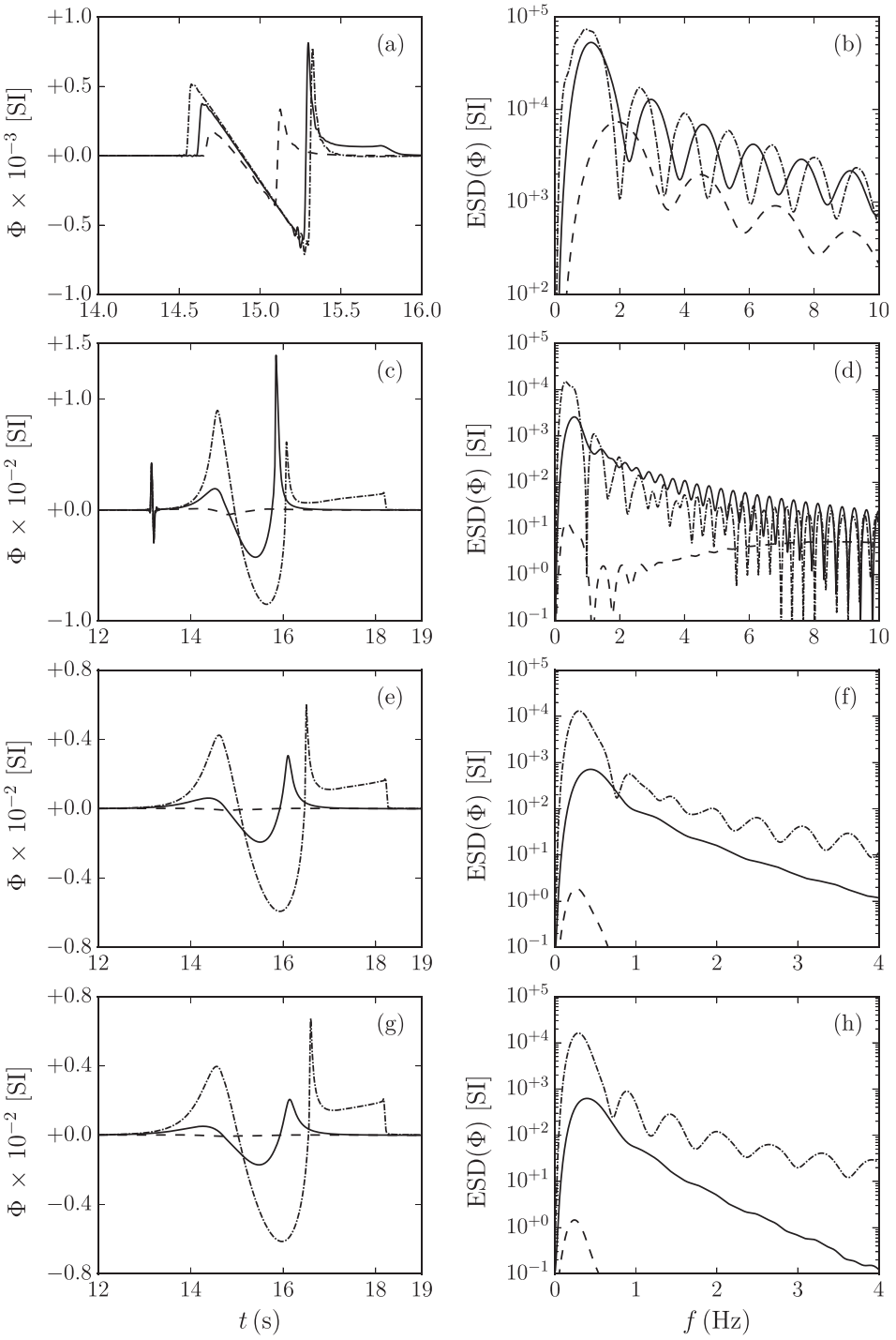

FIG. 5. Signals Φ synthesized at 5 km distance from the epicenter and corresponding one-sided energy spectral densities ESD(Φ) for (a) and (b) $\varphi_{NF} = 0^\circ$, (c) and (d) $\varphi_{NF} = 30^\circ$, (e) and (f) $\varphi_{NF} = 60^\circ$, and (g) and (h) $\varphi_{NF} = 90^\circ$: (dashed line) case NF10ktD, (solid line) case NF10kt, (dashed-dotted line) case NF10ktS.

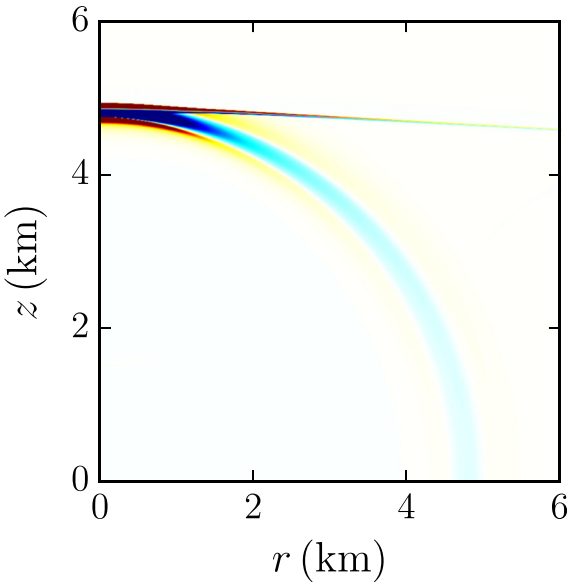

FIG. 6. (Color online) Scaled pressure field Φ obtained for case NF2013A at $t = 15$ s.

on the vertical axis. Moreover, the duration increases and the dominant frequency decreases as φ_{NF} increases to 90°. As an illustration, the fundamental frequencies for $\varphi_{NF} = 0°$ lie in the range [1 , 2 Hz], whereas they are lower than about 1 Hz for $\varphi_{NF} \geq 30°$.

B. Analysis of the results for the 2013 DPRK underground test

The scaled pressure perturbations Φ obtained in the case NF2013A at $t = 15$ s, are shown in Fig. 6. As in the previously-described simulations, the acoustic field appears as a superposition of a planar front, corresponding to the refracted P-wave, and of a quasi-spherical front emanating from the epicentral point. The planar wave is propagating upward with an angle with respect to the r-axis close to 90° so that it cannot be refracted back toward the ground.

The scaled pressure signals Φ obtained on the quasi-spherical front in the cases NF2013A and NF2013B at a distance $R_{NF} = \sqrt{r_{NF}^2 + z_{NF}^2}$ of 5 km from the epicenter and for zenith angles $\varphi_{NF} = \text{atan}(r_{NF}/z_{NF})$ equal to $\varphi_{NF} = 0°, 30°, 60°, 90°$, are reported in Fig. 7. The maximum overpressures for $\varphi_{NF} = 0°, 30°, 60°, 90°$ are, respectively, of about 661, 4.73, 1.08, and 0.88 $\text{Pa kg}^{-1/2}\,\text{m}^{3/2}$ in case NF2013A, and around 965, 17.9, 3.67, and 2.74 $\text{Pa kg}^{-1/2}\,\text{m}^{3/2}$ in case NF2013B. The corresponding characteristic periods, i.e., the temporal distance between the crests, are approximately equal to 0.6, 1.32, 2.06, and 2.35 s in simulation NF2013A, and to 0.72, 1.46, 2.14, and 2.42 s in simulation NF2013B. These results are summarized in Table III.

In order to help the understanding of the far-field results, the acoustic rays (Sabatini *et al.*, 2016b; Scott *et al.*, 2017) emanating from the aforementioned initial epicentral spherical front are plotted in Fig. 8. Well-formed tropospheric and stratospheric ducts are observed, mainly as a result of the presence of strong winds in the tropopause and in the stratopause. Only rays launched with an angle with respect to the r-axis lower than about 32° are trapped within the troposphere and the stratosphere. This result clearly demonstrates the importance of correctly reproducing the directivity pattern of underground explosions, since only the energy radiated within a shallow angle (of about 32° in the present case) can propagate at large range.

It is worth noting that thermospheric rays eventually reach the ground as well. However, due to the significant computational cost of simulations extending up to the lower thermosphere, they are not analyzed in this study.

The scaled pressure fields Φ obtained in the case FF2013–8kt at different instants of time, $t = t_1 = 100.5$ s, $t = t_2 = 301.5$ s, $t = t_3 = 469$ s, $t = t_4 = 636.5$ s, $t = t_5 = 804$ s,

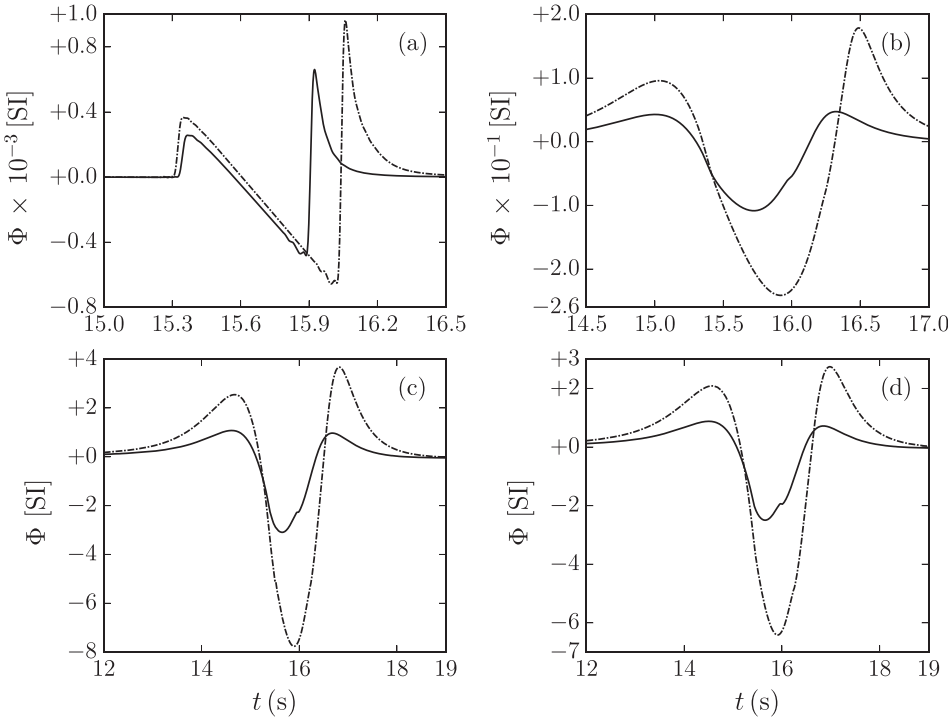

FIG. 7. Signals Φ obtained in the cases NF2013A and NF2013B at 5 km distance from the epicenter for (a) $\varphi_{NF} = 0°$, (b) $\varphi_{NF} = 30°$, (c) $\varphi_{NF} = 60°$, and (d) $\varphi_{NF} = 90°$: (black solid line) case NF2013A, (black dashed-dotted line) case NF2013B.

TABLE III. Characteristics of the signals obtained in simulations NF2013A and NF2013B, at a distance from the epicenter of $R_{NF} = \sqrt{r_{NF}^2 + z_{NF}^2} = 5$ km and for zenith angles $\varphi_{NF} = \text{atan}(r_{NF}/z_{NF})$ equal to $\varphi_{NF} = 0°, 30°, 60°, 90°$.

	Simulation	$\varphi_{NF} = 0°$	$\varphi_{NF} = 30°$	$\varphi_{NF} = 60°$	$\varphi_{NF} = 90°$
Maximum of	NF2013A	661	4.73	1.08	0.88
Φ (in SI units)	NF2013B	965	17.9	3.67	2.74
Characteristic	NF2013A	0.60	1.32	2.06	2.35
period (s)	NF2013B	0.72	1.46	2.14	2.42

$t = t_6 = 971.5$ s, $t = t_7 = 1139$ s, and $t = t_8 = 1293.1$ s, are displayed in Figs. 9(a)–9(h). The blue box represents the computational moving frame, whereas the black box indicates the physical domain of interest. Zooms of the acoustic fields observed at the times t_3, t_4, and t_7 are plotted in Panel 10 as well. Near the epicenter, the leading wavefront remains essentially spherical [cf. Fig. 9(a)]. However, as a result of the vertical gradients of the effective speed of sound, the acoustic wave is continuously deformed during its propagation. At the instant t_2, part of the wavefront has already been refracted back toward the Earth's surface within the troposphere [cf. Fig. 9(b)]. This portion of the acoustic front is called the *tropospheric phase*. At the time t_3, a *first stratospheric phase* is propagating back toward the ground [cf. Fig. 9(c)]. Moreover, leakage of acoustic energy from the tropospheric waveguide to the stratospheric duct is observed [cf. Figs. 9(c) and 10(a)]. More specifically, at about 7.92 km altitude, the tropospheric front seems to be partially transmitted in the stratosphere and partially reflected toward the ground. At the instant t_4, the first stratospheric phase has touched the terrestrial surface and is again traveling upward [cf. Fig. 9(d)]. Furthermore, the aforementioned leaked wave has reached the stratosphere and has been refracted downward [cf. Figs. 9(d) and 10(b)]. At the time t_5, the first stratospheric phase appears "split" into two different arrivals [cf. Fig. 9(e)]. As highlighted by Waxler *et al.* (2015) and Sabatini *et al.* (2015), among others, they are associated with lower (slow) and higher (fast) stratospheric rays (cf. Fig. 8). At the instant t_7, part of the acoustic front, after having traveled upward to the stratosphere [cf. Fig. 9(f)], is again propagating toward the ground [cf. Fig. 9(g)]. This portion of the acoustic front is here called the *second stratospheric phase*. Tropospheric downward refraction of the upward propagating first stratospheric phase is also visible (cf. Figs. 9(g) and 10(c)]. More generally, partial reflections are also observed whenever the wavefront travels downward or upward through the small-scale inhomogeneities of the effective-speed-of-sound profile (Sabatini *et al.*, 2019a). Finally, at the time t_8, the second stratospheric phase has just touched the ground.

The pressure perturbations p' computed at $r = 401$ km distance from the epicenter in the cases FF2013A, FF2013B, and FF2013AWR are illustrated in Fig. 11(a). The signals consist of three different arrivals: a tropospheric arrival, a tropospheric-stratospheric arrival, and a stratospheric arrival. The first and the last wavepackets propagate in the troposphere and in the stratosphere, respectively. The second arrival is a superposition of two main contributions: as also recognized by Assink *et al.* (2016), one component is due to the stratospheric downward refraction of the leaked tropospheric wave previously described; the other component, not identified by former investigators, is a consequence of the tropospheric downward refraction of the upward propagating stratospheric phase. Small-amplitude perturbations are observed as well between the two latest arrivals. They are associated with the partial reflections induced as the acoustic wavefront travels downward or upward through the small-scale inhomogeneities of the effective-speed-of-sound profile (Sabatini *et al.*, 2019a). As in the near-field zone, the amplitudes of the arrivals obtained with $Q = 16$ kt of trinitrotoluene (TNT) can be more than twice higher than those computed with $Q = 8$ kt of TNT. The vibrational relaxation of nitrogen N_2 and oxygen O_2 induces dispersion and dissipation. While the effect on the phase speed of the acoustic wave is practically negligible, these non-equilibrium phenomena lead to a reduction of amplitude as high as 14%. Their influence is more marked on the stratospheric arrival. As highlighted by Sabatini *et al.* (2016b), among others, such an impact is highest on waves with a period close to the relaxation times. Since the infrasonic signals under study have periods of about 0.5–2.5 s, the dissipation due to the vibrational relaxation of nitrogen N_2 and oxygen O_2 is maximal above the troposphere, between 20and 40 km altitude [cf. Fig. 2(c)]. For $z < 20$ km, the parameters $\bar{\Theta}_{N_2}$ and $\bar{\Theta}_{O_2}$ are too small for significant effects to be observed. It is worth mentioning that this conclusion would hold true even if the tropospheric humidity were considered in formulas [Eq. (9)] since humidity tends to further reduce the relaxation times (Pierce, 1978).

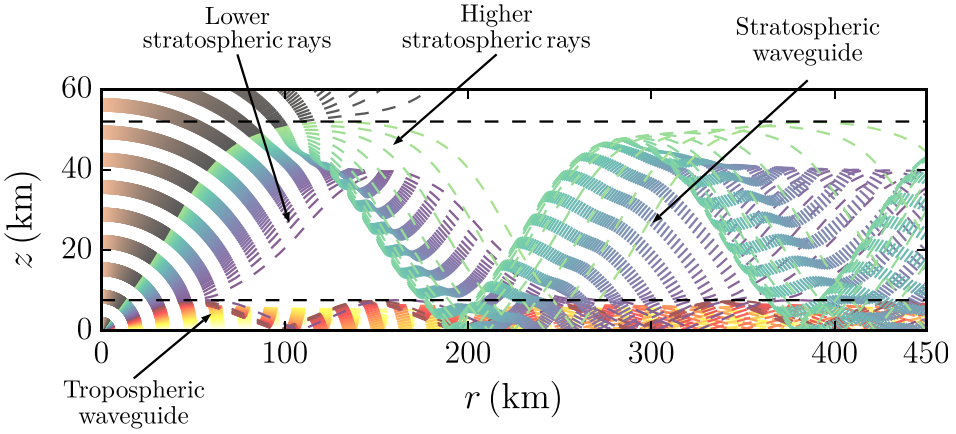

FIG. 8. (Color online) Acoustic rays associated with the speed-of-sound profile illustrated in Fig. 2.

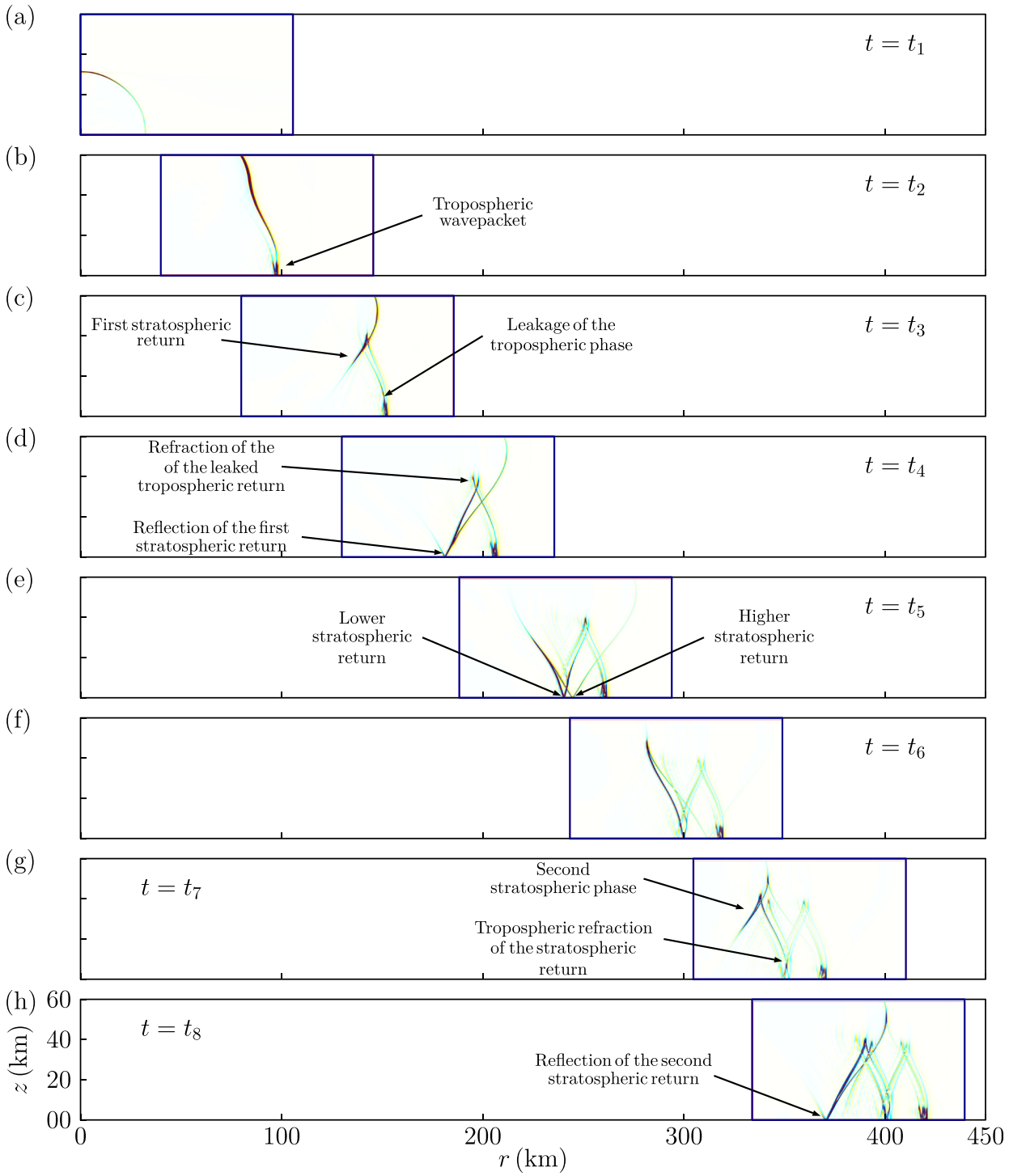

FIG. 9. (Color online) Scaled pressure fields Φ obtained in the case FF20138kt at different instants of time: (a) $t_1 = 100.5$ s, (b) $t_2 = 301.5$ s, (c) $t_3 = 469$ s, (d) $t_4 = 636.5$ s, (e) $t_5 = 804$ s, (f) $t_6 = 971.5$ s, (g) $t_7 = 1139$ s, and (h) $t_8 = 1293.1$ s.

The absolute value $P_w(t,f)$ of the time-frequency Morlet-wavelet transform of the ground pressure perturbation p' computed in the case of FF2013A at $r = 401$ km is displayed in Fig. 11(b). It is calculated as

$$P_w(t,f) = \left| \sqrt{f} \int_{-\infty}^{+\infty} p'(r = 401\ \text{km},\ z = 0\ \text{km}, \tau) \times \psi^\star(f(\tau - t)) d\tau \right|, \tag{20}$$

where $\psi^\star$ is the complex conjugate of the wavelet ψ. The mother Morlet wavelet is here defined by the following formula:

$$\psi(t) = \pi^{-1/4} \left(e^{i2\pi t} - e^{-2\pi^2/2} \right) e^{-t^2/2}. \tag{21}$$

The diagram clearly shows that the energy of the three arrivals is mostly contained in frequencies lower than about 2 Hz.

The signals p' synthesized at $r = 401$ km distance from the epicenter in the cases FF2013A and FF2013B can be

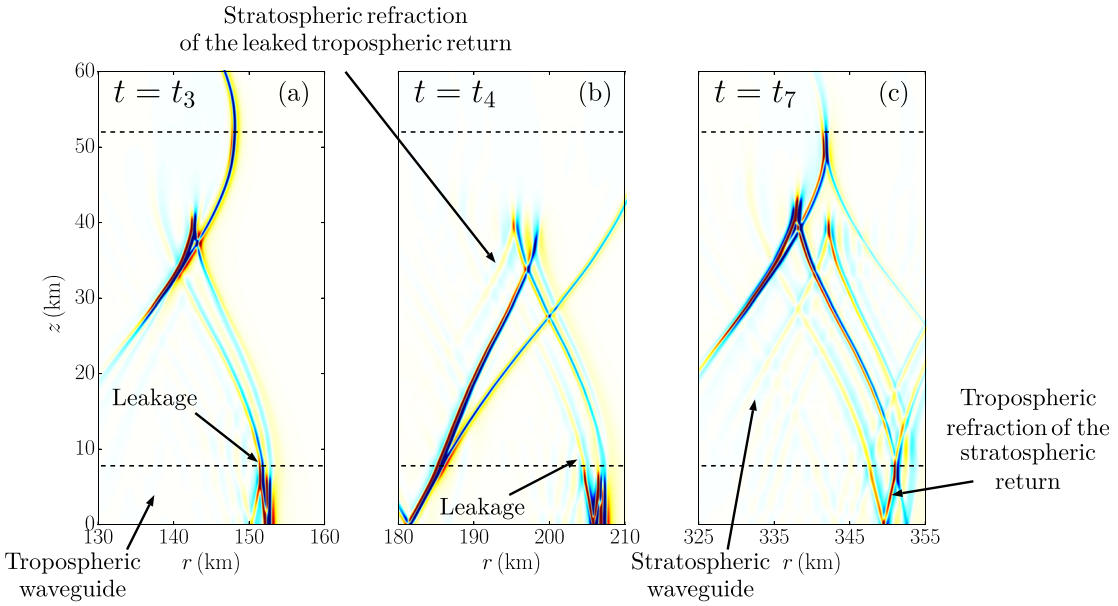

FIG. 10. (Color online) Zooms of the scaled pressure fields Φ obtained in the case FF20138kt at the times (a) $t_3 = 469$ s, (b) $t_4 = 636.5$ s, and (c) $t_7 = 1139$ s.

qualitatively compared with the pressure perturbations recorded at the I45RU station of the IMS after the 2013 DPRK test and reported in Fig. 4 of Assink *et al.* (2016). Good agreement between data and numerical results is found for the arrival times. The amplitudes of the recorded tropospheric and of the tropospheric-stratospheric wavepackets are clearly close to those of the corresponding arrivals synthesized in simulation FF2013A. The amplitude of the stratospheric wavepacket is however slightly overestimated by the numerical simulation. The different discrepancies could be attributed to various factors: the topography (de Groot-Hedlin, 2017), the horizontal variability of the mean atmosphere, and the ubiquitous presence of turbulent fluctuations (Sabatini *et al.*, 2019b). A more accurate method to simulate the radiation of infrasound from underground explosions could also lead to improved comparisons.

V. CONCLUDING REMARKS

The long-range propagation of infrasonic waves generated by underground explosions is investigated by performing direct numerical simulations of the equations of fluid dynamics. The 3D axisymmetric continuity, momentum, and energy conservation equations are more particularly solved, along with the Herzfeld-Rice equations that

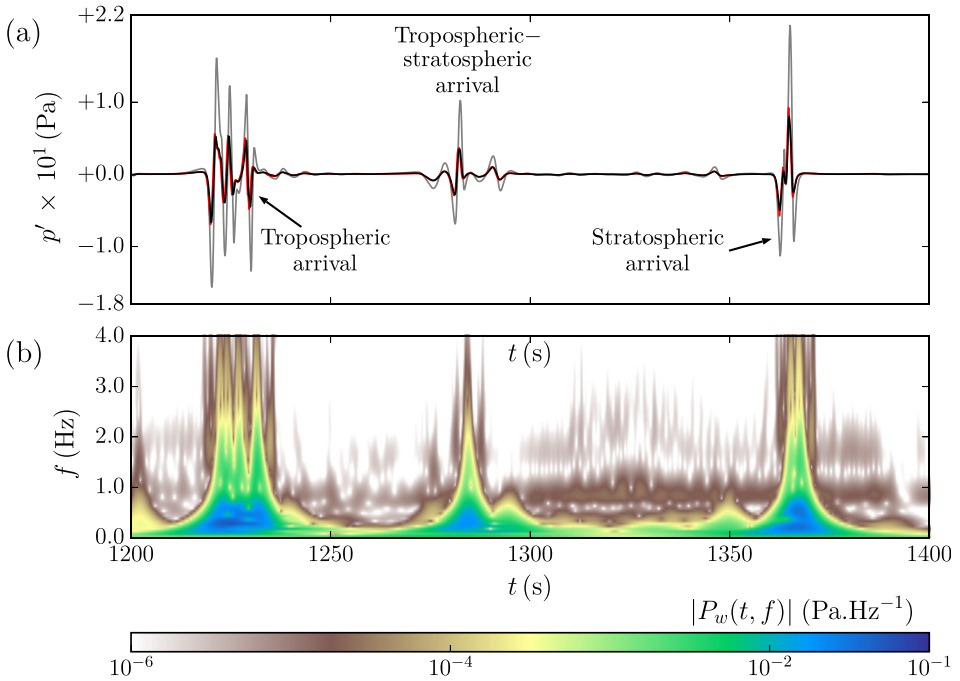

FIG. 11. (Color online) (a) Ground signals p' obtained at $r = 401$ km in the cases (black line) FF2013A, (gray line) FF2013B, and (red line) FF2013AWR (without relaxation effects). (b) Absolute value $|P_w(t,f)|$ of the Morlet wavelet transform of the ground signal obtained at $r = 401$ km in case FF2013A.

describe the absorption and the dispersion induced by vibrational relaxation phenomena. The radiation of acoustic energy by the ground motion produced by underground explosions is initiated by enforcing the equality, at ground level, between the component of the air velocity normal to the Earth's surface and the normal velocity of the ground layer. The velocity of the ground layer is defined by using well-known semi-empirical formulas. Eleven direct numerical simulations are carried out through a high-order low-dispersive and low-dissipative finite-difference time-domain method.

The acoustic perturbations obtained near the epicenter of an underground test are first analyzed. The atmospheric pressure field appears as a superposition of two distinct fronts: a planar front and a quasi-spherical wave emanating from the epicentral point. The former is associated with the refraction in the atmosphere of the wave-induced by the buried explosion which is propagating horizontally along the ground layer; furthermore, it is traveling in a direction nearly parallel to the vertical axis, so that it cannot be refracted back toward the ground in the tropospheric and stratospheric ducts. The latter is the sole that can be observed on the Earth's surface at a long range. Moreover, it is found that most of the energy radiated in the atmosphere is directed upward, and only a small percentage of it can travel a large distance through the atmospheric waveguides. As an illustration, the present results suggest that the signals propagating along the vertical direction could have amplitudes tens to hundreds of times higher than those detected on stratospheric rays, which travel at angles with respect to the horizontal axis lower than about 30°.

An analysis of the infrasonic signal recorded at the I45RU station of the International Monitoring System after the test conducted in North Korea on 12 February 2013 is then realized. Three different arrivals are identified. The first and the last detected wavepackets are ducted in the troposphere and in the stratosphere, respectively. The tropospheric and the stratospheric waveguides are created by strong wind jets located at about 8 and 53 km altitude, respectively. The present results indicate that the second arrival could be due to a superposition of two different contributions, not clearly identified by former investigators: on one hand, acoustic energy leaks from the tropospheric waveguide to the stratospheric one and is then carried back toward the ground; the stratospheric phase, tunneled between the ground and the stratosphere, is refracted back toward the Earth's surface as it travels upward through the tropospheric wind jet. Furthermore, the vibrational relaxation of nitrogen N_2 and oxygen O_2 is found to have an appreciable impact on the ground recording, especially on the stratospheric arrival, by leading to an amplitude reduction as high as 14% in the configuration under study.

A qualitative comparison between data (reported in Assink *et al.*, 2016) and synthesized waveforms is additionally carried out. A good agreement is found for the arrival times of the aforementioned wavepackets. Moreover, the amplitudes of the recorded tropospheric and of the tropospheric-stratospheric arrivals seem to indicate that the source yield of the 2013 DPRK test could be closer to 8 kt of TNT than to 16 kt of TNT. Since the effects of the topography and of the spatio-temporal variability of the atmospheric mean state, among others, are not taken into account in this work, a definitive quantification of the source yield for the 2013 DPRK test is here precluded. Nevertheless, the results described in this paper certainly motivate the use of infrasound technologies, alongside with seismic techniques, as tools for the characterization of underground explosions. In this context, a possible extension of the present investigation consists in analyzing the portion of the acoustic front which propagates upward toward the thermosphere and the ionosphere, inducing perturbations of the electron density which can be eventually detected through the global navigation satellite system (GNSS) (Park *et al.*, 2013; Yang *et al.*, 2012).

To conclude, in order to allow more quantitative comparisons with measurements, different improvements to the present modeling are required: first, a better description of the explosive source and of the coupling between the ground and the atmosphere is needed; second, a real topography must be implemented in the algorithm, since it potentially affects both the radiation pattern and the propagation in the tropospheric waveguide; finally, three-dimensional space- and time-dependent mean atmospheric fields have to be considered, as they influence the waveform, the amplitude, and the spectrum of the infrasonic arrivals.

ACKNOWLEDGMENTS

The authors acknowledge support from the Defense Threat Reduction Agency Award No. HDTRA1-16-1-0046 to Purdue University via a sub-award to the Embry-Riddle Aeronautical University. The authors also gratefully acknowledge the use of the ERAU Vega High-Performance Computing Cluster and the assistance of Scott Hicks.

APPENDIX A; ACCURACY OF THE TIME INTEGRATION ALGORITHM FOR THE RELAXATION EQUATIONS

As highlighted by Hanique-Cockenpot (2011), including the relaxation phenomena in the classical system of equations of fluid dynamics may impose a constraint on the maximum time-step Δt allowed for accurate and stable numerical simulations. In order to address this issue, the following representative ordinary differential equation is considered:

$$\frac{dU}{dt} = -\frac{U}{\Theta}, \tag{A1}$$

where U is the unknown function and Θ is a relaxation time. The exact amplification factor $\mathcal{G}$ between the instant t^n and $t^{n+1} = (t^n + \Delta t)$ is given by the expression

$$\mathcal{G} \equiv \frac{U^{n+1}}{U^n} = e^{-\Delta t/\Theta}, \tag{A2}$$

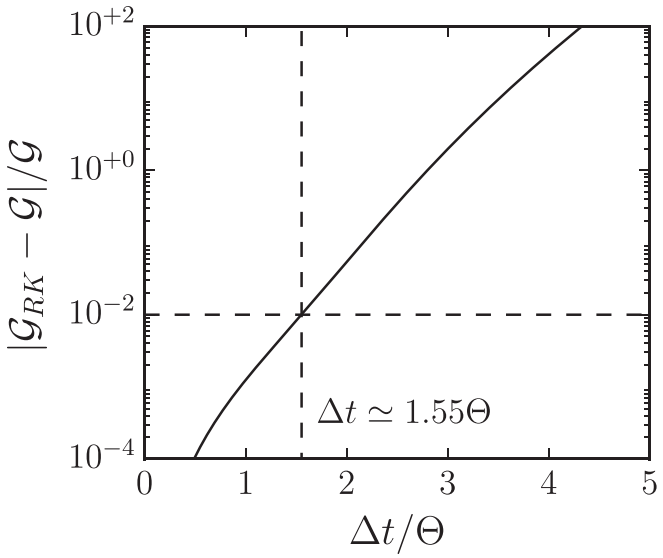

FIG. 12. Numerical error for the time integration of the relaxation equations as a function of the ratio between the time step Δt and the generic relaxation time Θ.

where $U^p = U(t^p)$. The time-integration algorithm employed in this work can be developed as (Bogey and Bailly, 2004)

$$U_{\mathrm{a}}^{n+1} = U^n + \sum_{j=1}^{6} \Gamma_j \Delta t^j \frac{d^j U^n}{dt^j}, \tag{A3}$$

where U_{a}^{n+1} is the approximated numerical solution at the instant t^{n+1} and $\Gamma_j, j = 1, \ldots, 6$, are known coefficients. Since

$$\frac{d^j U^n}{dt^j} = (-1)^j \frac{U^n}{\Theta^j}, \tag{A4}$$

the numerical amplification factor $\mathcal{G}_{RK}$ is equal to

$$\mathcal{G}_{RK} \equiv \frac{U_a^{n+1}}{U^n} = 1 + \sum_{j=1}^{6} (-1)^j \Gamma_j \left(\frac{\Delta t}{\Theta}\right)^j. \tag{A5}$$

The relative error $|\mathcal{G}_{RK} - \mathcal{G}|/\mathcal{G}$ is plotted in Fig. 12 as a function of the parameter $\Delta t/\Theta$ and is shown to remain lower than 1% for $\Delta t < 1.55\,\Theta$. Finally, the present time integration algorithm is found to be unstable for values of Δt higher than about $4.15\,\Theta$, for which the factor $\mathcal{G}_{RK}$ becomes greater than 1.

APPENDIX B: CONVERGENCE ANALYSIS

In order to illustrate the capability of the present algorithm, the effect of the spatial resolution is here reported. The signals Φ computed in the cases NF2013A, NF2013A4m, and FF2013A, at a distance $R_{\mathrm{NF}} = \sqrt{r_{\mathrm{NF}}^2 + z_{\mathrm{NF}}^2}$ of 5 km from the epicenter and for zenith angles $\varphi_{\mathrm{NF}} = \mathrm{atan}(r_{\mathrm{NF}}/z_{\mathrm{NF}})$ equal to $\varphi_{\mathrm{NF}} = 0°, 30°, 60°, 90°$, are shown in Fig. 13. On the vertical axis, for $\varphi_{\mathrm{NF}} = 0°$, an N-wave is obtained. While the front and rear shocks are not well resolved, their positions, as well as the central part of the N-wave, are correctly calculated even on the coarsest grid. For $\varphi_{\mathrm{NF}} = 30°, 60°$, and 90°, the results obtained with the three spatial resolutions are practically superimposed. As stated in Sec. IV B, only the acoustic rays launched with an angle with respect to the r-axis lower than about 32° are refracted back toward the ground in the troposphere and in the stratosphere. Consequently, the coarsest grid spacing $\Delta r = \Delta z = 8$ m, which is the minimum allowed by the memory of the GPU employed in this work, provides very accurate computations in the far-field cases.

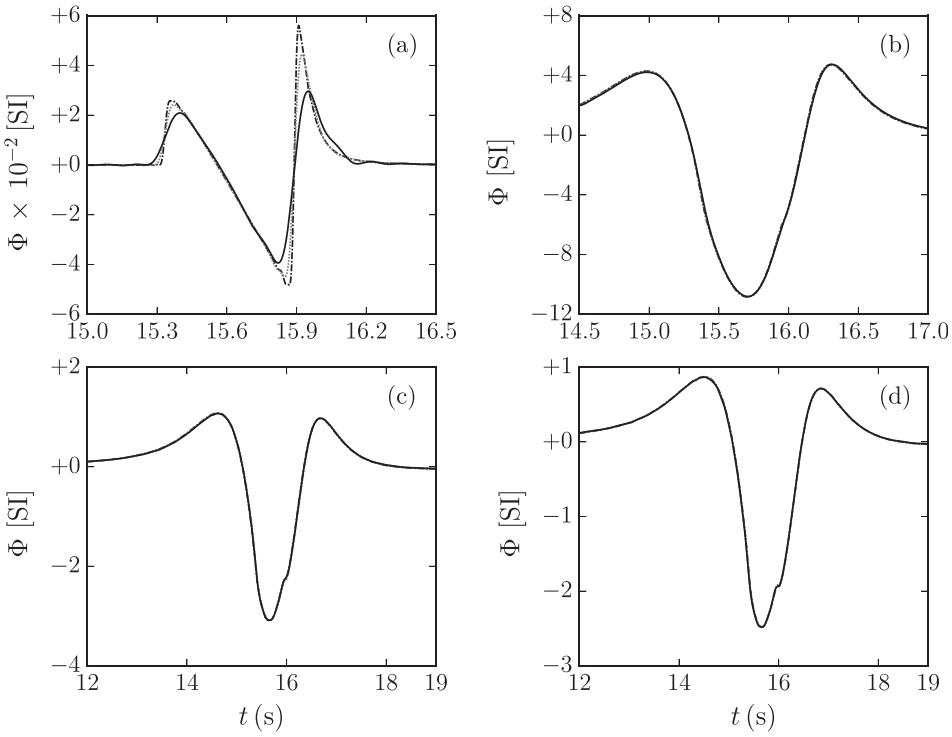

FIG. 13. Signals Φ computed in the cases NF2013A, NF2013A4m, and FF2013A, at a distance $R_{\mathrm{NF}} = \sqrt{r_{\mathrm{NF}}^2 + z_{\mathrm{NF}}^2}$ of 5 km from the epicenter and for zenith angles $\varphi_{\mathrm{NF}} = \mathrm{atan}(r_{\mathrm{NF}}/z_{\mathrm{NF}})$ equal to (a) 0°, (b) 30°, (c) 60°, and (d) 90°: (black dashed-dotted line) $\Delta r = \Delta z = 2$ m (case NF2013A), (gray dashed line) $\Delta r = \Delta z = 4$ m (case NF2013A4m), (black solid line) $\Delta r = \Delta z = 8$ m (case FF2013A).

Adushkin, V. V., and Spivak, A. (**2015**). "Underground explosions," Technical Report WGC-2015-03, translated from Russian to English by A. Stroujkova and P. Richards.

Assink, J. D., Averbuch, G., Smets, P. S. M., and Evers, L. G. (**2016**). "On the infrasound detected from the 2013 and 2016 DPRK's underground nuclear tests," Geophys. Res. Lett. **43**(7), 3526–3533, https://doi.org/10.1002/2016GL068497.

Bailly, C., and Bogey, C. (**2009**). "Direct computation of infrasound propagation in inhomogeneous atmosphere using a low-dispersion and low-dissipation algorithm," in *Computational Fluid Dynamics 2008*, edited by H. Choi, H. G. Choi, and J. Y. Yoo (Springer Berlin-Heidelberg), pp. 113–118.

Berland, J., Bogey, C., and Bailly, C. (**2007**). "High-order, low dispersive and low dissipative explicit schemes for multi-scale and boundary problems.," J. Comput. Phys. **224**(2), 637–662.

Blom, P. (**2019**). "Modeling infrasonic propagation through a spherical atmospheric layer—Analysis of the stratospheric pair," J. Acoust. Soc. Am. **145**(4), 2198–2208.

Bogey, C., and Bailly, C. (**2002**). "Three-dimensional non-reflective boundary conditions for acoustic simulations: Far-field formulation and validation test cases," Acta Acust. united Ac. **88**, 463–471.

Bogey, C., and Bailly, C. (**2004**). "A family of low dispersive and low dissipative explicit schemes for noise computations.," J. Comput. Phys. **194**(1), 194–214.

Bogey, C., Cacqueray, N. D., and Bailly, C. (**2009**). "A shock-capturing methodology based on adaptive spatial filtering for high-order nonlinear computations.," J. Comput. Phys. **228**, 1447–1465.

Campus, P., and Christie, D. R. (**2009**). *Worldwide Observations of Infrasonic Waves* (Springer, Dordrecht, the Netherlands), pp. 185–234.

Che, I.-Y., Park, J., Kim, I., Kim, T. S., and Lee, H.-I. (**2014**). "Infrasound signals from the underground nuclear explosions of North Korea," Geophys. J. Int. **198**(1), 495–503.

Cramer, M. S. (**2012**). "Numerical estimates for the bulk viscosity of ideal gases," Phys. Fluids **24**(6), 066102.

de Groot-Hedlin, C. D. (**2012**). "Nonlinear synthesis of infrasound propagation through an inhomogeneous, absorbing atmosphere," J. Acoust. Soc. Am. **132**(2), 646–656.

de Groot-Hedlin, C. D. (**2016**). "Long-range propagation of nonlinear infrasound waves through an absorbing atmosphere," J. Acoust. Soc. Am. **139**(4), 1565–1577.

de Groot-Hedlin, C. D. (**2017**). "Infrasound propagation in tropospheric ducts and acoustic shadow zones," J. Acoust. Soc. Am. **142**(4), 1816–1827.

Drob, D. P., Picone, J. M., and Garcés, M. (**2003**). "Global morphology of infrasound propagation," J. Geophys. Res. **108**(D21), 4680, https://doi.org/10.1029/2002JD003307.

Glasstone, S., and Dolan, P. J. (**1977**). *The Effects of Nuclear Weapons*, 3rd ed. (Department of Defense, Washington, DC).

Godin, O. A. (**2002**). "An effective quiescent medium for sound propagating through an inhomogeneous, moving fluid," J. Acoust. Soc. Am. **112**(4), 1269–1275.

Hanique-Cockenpot, G. (**2011**). "Etude numérique de la propagation non linéaire des infrasons dans l'atmosphère" ("A numerical study of the nonlinear propagation of infrasonic waves in the atmosphere"), Ph.D. thesis, École Centrale de Lyon, Lyon, France.

Jones, K. R., Whitaker, R. W., and Arrowsmith, S. J. (**2015**). "Modelling infrasound signal generation from two underground explosions at the Source Physics Experiment using the Rayleigh integral," Geophys. J. Int. **200**(2), 779–790.

Koch, K., and Pilger, C. (**2018**). "Infrasound observations from the site of past underground nuclear explosions in North Korea," Geophys. J. Int. **216**(1), 182–200.

Krasnov, V., and Drobzheva, Y. (**2005**). "The acoustic field in the ionosphere caused by an underground nuclear explosion," J. Atmos. Solar Terr. Phys. **67**(10), 913–920.

Lee, H., and Walker, J. J. (**1980**). "Model for ground motion and atmospheric overpressure due to underground nuclear explosion," Technical Report LA-8554-MS (Los Alamos Scientific Laboratory, Los Alamos, NM).

Li, X.-D., Hu, Z.-M., and Jiang, Z.-L. (**2017**). "Continuum perspective of bulk viscosity in compressible fluids," J. Fluid Mech. **812**, 966–990.

Marsden, O., Bogey, C., and Bailly, C. (**2014**). "A study of infrasound propagation based on high-order finite difference solutions of the Navier-Stokes equations," J. Acoust. Soc. Am. **135**(3), 1083–1095.

Mohseni, K., and Colonius, T. (**2000**). "Numerical treatment of polar coordinate singularities," J. Comput. Phys. **157**(2), 787–795.

Park, J., Che, I.-Y., Stump, B., Hayward, C., Dannemann, F., Jeong, S., Kwong, K., McComas, S., Oldham, H. R., Scales, M. M., and Wright, V. (**2018**). "Characteristics of infrasound signals from North Korean underground nuclear explosions on 2016 January 6 and September 9," Geophys. J. Int. **214**(3), 1865–1885.

Park, J., Helmboldt, J., Grejner-Brzezinska, D. A., von Frese, R. R. B., and Wilson, T. L. (**2013**). "Ionospheric observations of underground nuclear explosions (UNE) using GPS and the very large array," Radio Sci. **48**(4), 463–469, https://doi.org/10.1002/rds.20053.

Pierce, A. D. (**1978**). "Aeroacoustic fluid dynamic equations and their acoustic energy conservation corollary with O2 and N2 vibrational relaxation effects included," J. Sound Vib. **58**(2), 189–200.

Pierce, A. D. (**2019**). *Acoustics. An Introduction to its Physical Principles and Applications* (Springer International Publishing, New York).

Rodean, H. C. (**1970**). "Explosion-produced ground motion: Technical summary with respect to seismic hazards," CONF-700101, vol 2; INIS-XA-N-229. Symposium on Engineering with Nuclear Explosives, 14–16 January 1970, Las Vegas, NV.

Rudenko, G., and Uralov, A. M. (**1995**). "Calculation of ionospheric effects due to acoustic radiation from an underground nuclear explosion," J. Atmos. Terres. Phys. **57**(3), 225–236.

Sabatini, R., Marsden, O., Bailly, C., and Bogey, C. (**2016a**). "A numerical study of nonlinear infrasound propagation in a windy atmosphere," J. Acoust. Soc. Am. **140**(1), 641–656.

Sabatini, R., Marsden, O., Bailly, C., and Gainville, O. (**2015**). "Numerical simulation of infrasound propagation in the earth's atmosphere: Study of a stratospherical arrival pair," AIP Conf. Proc. **1685**(1), 090002.

Sabatini, R., Marsden, O., Bailly, C., and Gainville, O. (**2016b**). "Characterization of absorption and non-linear effects in infrasound propagation using an augmented burgers' equation," Geophys. J. Int. **207**, 1432–1445.

Sabatini, R., Marsden, O., Bailly, C., and Gainville, O. (**2019a**). "Three-dimensional direct numerical simulation of infrasound propagation in the Earth's atmosphere," J. Fluid Mech. **859**, 754–789.

Sabatini, R., Snively, J. B., Bailly, C., Hickey, M. P., and Garrison, J. L. (**2019b**). "Numerical modeling of the propagation of infrasonic acoustic waves through the turbulent field generated by the breaking of mountain gravity waves," Geophys. Res. Lett. **46**(10), 5526–5534, https://doi.org/10.1029/2019GL082456.

Salomons, E. M., Blumrich, R., and Heimann, D. (**2002**). "Eulerian time-domain model for sound propagation over a finite-impedance ground surface. comparison with frequency-domain models," Acta Acust. united Ac. **88**(4), 483–492.

Scott, J., Blanc-Benon, P., and Gainville, O. (**2017**). "Weakly nonlinear propagation of small-wavelength, impulsive acoustic waves in a general atmosphere," Wave Motion **72**, 41–61.

Snively, J. B. (**2013**). "Mesospheric hydroxyl airglow signatures of acoustic and gravity waves generated by transient tropospheric forcing," Geophys. Res. Lett. **40**(17), 4533–4537, https://doi.org/10.1002/grl.50886.

Sutherland, L. C., and Bass, H. E. (**2004**). "Atmospheric absorption in the atmosphere up to 160 km," J. Acoust. Soc. Am. **115**(3), 1012–1032.

Sutherland, L. C., and Bass, H. E. (**2006**). "Erratum: Atmospheric absorption in the atmosphere up to 160 km," J. Acoust. Soc. Am. **120**(5), 2985.

Voytan, D. P., Lay, T., Chaves, E. J., and Ohman, J. T. (**2019**). "Yield estimates for the six North Korean nuclear tests from teleseismic P wave modeling and intercorrelation of P and Pn recordings," J. Geophys. Res. Solid Earth **124**(5), 4916–4939, https://doi.org/10.1029/2019JB017418.

Waxler, R., Evers, L. G., Assink, J., and Blom, P. (**2015**). "The stratospheric arrival pair in infrasound propagation," J. Acoust. Soc. Am. **137**(4), 1846–1856.

Whitaker, R. W. (**2007**). "Infrasound signals as basis for event discriminants," in *Proceedings of the 29th Monitoring Research Review: Ground-Based Nuclear Explosion Monitoring Technologies*, September 25–27, Denver, CO.

Whitaker, R. W. (**2008**). "Infrasound signals from ground-motion sources," in *Proceedings of the 30th Monitoring Research Review: Ground-Based Nuclear Explosion Monitoring Technologies*, September 23–25, Portsmouth, VA.

Yang, Y.-M., Garrison, J. L., and Lee, S.-C. (**2012**). "Ionospheric disturbances observed coincident with the 2006 and 2009 North Korean underground nuclear tests," Geophys. Res. Lett. **39**(2), L02103, https://doi.org/10.1029/2011GL050428.

Zettergren, M. D., and Snively, J. B. (**2019**). "Latitude and longitude dependence of ionospheric tec and magnetic perturbations from infrasonic-acoustic waves generated by strong seismic events," Geophys. Res. Lett. **0**(0), 1132–1140, https://doi.org/10.1029/2018GL081569.

Zhang, M., and Wen, L. (**2013**). "High-precision location and yield of North Korea's 2013 nuclear test," Geophys. Res. Lett. **40**(12), 2941–2946, https://doi.org/10.1002/grl.50607.